Atomization Mechanism of Internally Mixing Twin-Fluid Y-Jet Atomizer

Y. H. Nazeer[1*], M. Ehmann[1], M. Sami[2], M. Gavaises[3]

[1]Mitsubishi Hitachi Power Systems Europe GmbH, Germany
[2]ANSYS, Inc., Houston, Texas, USA
[3]School of Mathematics, Computer Sciences and Engineering, City, University of London, UK

Abstract

The atomization mechanism of the gas-liquid multiphase flow through internally mixing twin-fluid Y-jet atomizer has been studied by examining both the internal and external flow patterns. Super-heated steam and Light Fuel Oil (LFO) are used as working fluids. The flow is numerically modeled using the compressible Navier-Stokes equations; hybrid Large Eddy Simulation approach through Wall Modeled Large Eddy Simulations (WMLES) is used to resolve the turbulence with the Large Eddy Simulations, whereas the Prandtl Mixing Length Model is used for modeling the subgrid-scale structures, which are affected by operational parameters. VOF-to-DPM transition mechanism is utilized along with dynamic solution-adaptive mesh refinement to predict the initial development and fragmentation of the gas-liquid interface through Volume-of-Fluid (VOF) formulations on a sufficiently fine mesh, while Discrete Phase Model (DPM) is used to predict the dispersed part of the spray on the coarser grid. Two operational parameters, namely gas-to-liquid mass flow rate ratio (GLR) and liquid-to-gas momentum ratio are compared; the latter is found to be an appropriate operational parameter to describe both the internal flow and atomization characteristics. It is confirmed that the variation in the flow patterns within the mixing-port of the atomizer coincides with the variation of the spatial distribution of the spray drops.

Keywords: Internally Mixing Twin-Fluid Y-Jet Atomizer, VOF-to-DPM, Wall Modeled Large Eddy Simulations (WMLES)

Nomenclature

Acronyms

SMD	Sauter Mean Diameter
VOF	Volume of Fluid
HPC	High-Performance Computing
WMLES	Wall Modeled Large Eddy Simulations
LES	Large Eddy Simulations
RANS	Reynolds-Averaged Navier-Stokes
DPM	Discrete Phase Model
SGS	Subgrid Scale
Eq.	Equation
HPC	High Performance Computing

Subscripts

p	Phase p
q	Phase q
m	Mixing Port
M	Mixing Point
g	Gas
l	Liquid
pz	Premix Zone
r	relative
pr	Particle
max	Maximum

min	Minimum

Superscript

T	Transpose
s	Sub-grid Scale

Symbols

α	Volume Fraction
ρ	Density, kg/m^3
V	Velocity, m/s
P	Pressure, Pa
μ	Viscosity, $kg/m.s$
g	Gravitational Acceleration, m/s^2
T_σ	Surface Tension Force, N
T	Temperature, K
k	Curvature, m^{-1}
σ	Surface Tension, N/m
E	Energy, J
K_∞	Thermal Conductivity, $W/m.K$
K_{eff}	Effective Thermal Conductivity, $W/m.K$
Δ	Modified Length Scale, m
τ_{ij}	Viscous Stress, N/m^2
ν_t	Eddy Viscosity, m^2/s
δ_{ij}	Kronecker Delta
y^+	Dimensionless Wall Distance
Ω	Vorticity, s^{-1}

S	Strain Rate, s^{-1}
θ	Angle, °
l	Length, mm
d	Diameter, m
τ_{kk}	Isotropic Part of the Subgrid Stress, N/m^2
φ	Momentum Ratio
M	Mass Flow Rate, kg/s
G	Mass Velocity, $kg/m^2 s$
C_w	Empirical Constant
h_{max}	Maximum Edge Length, m
h_{wn}	Grid Step in Wall Normal Direction, m
d_w	Distance from Wall, m
C_{smag}	Smagorinsky Constant
a_1	Constant defined in Eq. 11
a_2	Constant defined in Eq. 11
a_3	Constant defined in Eq. 11
C_D	Drag Coefficient
F_D	Drag Force Per Unit Mass, N/kg
Ar	Surface Area, m^2
h	Convective Heat Transfer Coefficient, W/Km^2
Y	Coordinate Axis
C	Heat Capacity, J/K

26

27

28

Introduction

The description of "twin-fluid atomizer" can be applied to any nozzle in which the driving force for the liquid jet break up is air, steam or any gas. Twin-fluid atomizers could be classified into "air-assist," "airblast" and "effervescent" atomizers (Lefebrve, 1992). One thing common between different types of twin-fluid air-assist atomizers (Mlkvik, et al., 2015), (Pacifico & Yanagihara, 2014) and (Kufferath, et al., 1999) and airblast atomizers (Inamura, et al., 2019), (Okabe, et al., 2019) and (Roudini & Wozniak, 2018) is that the bulk liquid to be atomized is first transformed into a jet or sheet before being exposed to high-velocity gas. In contrast, in effervescent atomizers (Roesler & Lefebvre, 1989), (Buckner, et al., 1990a), (Buckner, et al., 1990b) and (Sovani, et al., 2001) the atomizing gas is injected into the bulk liquid at low velocity to form a bubbly two-phase mixture upstream of the discharge orifice. The main difference between the air-assist and airblast atomizers is that the former employs high pressure source of air or steam at very high velocities (usually sonic) and at relatively smaller mass flow rates while the latter employ low pressure gas source and much larger amount of gas flow at relatively lower velocities (Lefebrve, 1992) and (Lefebvre, 1980).

Air-assist atomizers can be classified into internal-mixing and external-mixing types. In the former, high velocity air or steam impinges on the liquid jet within the mixing chamber of the nozzle while in the latter the air or steam impinges on the liquid sheet or jet outside the discharge orifice. In the external mixing type, the spray cone angle is minimum for the maximum gas flow, and the spray widens as the gas flow is reduced; whereas external mixing type can be designed to give constant spray angle at all liquid flow rates. Internal mixing air-assist atomizers are highly suitable for high viscous liquids, as good atomization can be achieved down to very low liquid mass flow rates (Barreras, et al., 2008).

In large oil-fired industrial boilers or thermal power plants, either Y-jet atomizers or internal mixing chamber twin-fluid atomizers are used (Barreras, et al., 2006). The former is usually used with light fuel oil while the latter is used with heavy fuel oil and steam as auxiliary fluid (Li, et al., 2012). The

54 characteristics of the Y-jet atomizer is that the liquid and gas (air or steam) are mixed before injected

55 out. It generally consists of a number of jets, from a minimum of two to maximum of 20, arranged

56 annularly to provide a hollow conical spray. In each individual 'Y', oil is injected into the mixing port,

57 where it mixes with the atomizing fluid (steam or air) admitted through the gas port. The mixing

58 ports are uniformly spaced around the atomizer body at an angle to the nozzle axis (see Figure 1) so

59 that the individual jets of two-phase mixture emanating from the mixing ports rapidly merge to form

60 a hollow conical spray.

61 The spraying performance (expressed by the mean droplet size) of the Y-jet atomizer is reported to

62 be affected by properties of gas and liquid, injection pressure, and also by the geometric

63 configurations such as the mixing-port size and the intersecting angle between the liquid and gas

64 ports. Mullinger and Chigier (Mullinger & Chigier, 1974) and Prasad (Prasad, 1982) studied the effect

65 of geometric parameters on the mean drop size and suggested the design criteria to generate the

66 fine droplets. Song and Lee (Song & Lee, 1994) conducted the experimental examination, with water

67 and air as test fluids, to study the effect of mixing port length on the Y-jet atomizer's spray

68 performance. They concluded that the mean droplet size decreases and becomes spatially even as

69 the mixing port length is reduced. In a classical study, with water and air as working fluids, Song and

70 Lee (Song & Lee, 1996) studied the atomization mechanism of the gas-liquid mixture flowing through

71 internally mixing twin-fluid Y-jet atomizer by examining both the internal and external nozzle flow

72 patterns. They compared two operational parameters, namely gas-to-liquid mass flow rate ratio

73 (GLR) and liquid-to-gas momentum ratio to describe the internal flow patterns and external drop size

74 distribution. The atomization model of Y-jet atomizer proposed by Mullinger and Chigier (Mullinger &

75 Chigier, 1974), Song and Lee (Song & Lee, 1996) and Andreussi et al. (Andreussi, et al., 1992) is

76 almost the same. The main difference is that the internal atomization mechanism proposed by Song

77 and Lee is subdivided into two parts namely direct collision mode and entrainment/deposition mode.
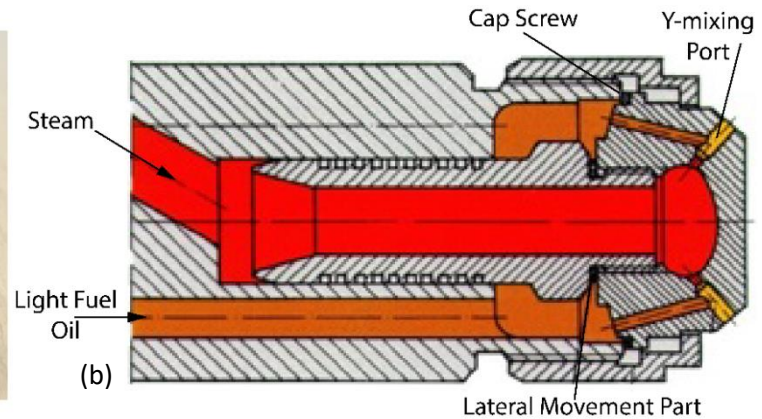
78

Figure 1 (a) Nozzle head of twin fluid Y-jet atomizer (b) Schematic of internally mixing twin-fluid Y-jet atomizer.

There are few studies predicting the internal flow characteristics, flow rates and energy required for the atomization (Nazeer, et al., 2019), (De Michele, et al., 1991), (Andreussi, et al., 1994), (Andreussi, et al., 1992) and (Song & Lee, 1994). There also exist several studies on the atomization characteristics of twin-fluid Y-jet atomizers (Song & Lee, 1996), (Mullinger & Chigier, 1974), (Neya, et al., 1975), and (Andreussi, et al., 1994); parameters such as atomizer geometry and injection conditions were taken as "input" and the spray performance was considered as "output." However, the effect of internal flow conditions on the atomization characteristics is not reported in detail. The effect of internal flow condition can be understood only by looking into both the internal flow patterns and the atomization mechanism simultaneously. (Neya, et al., 1975), (Andreussi, et al., 1994) and (Song & Lee, 1996) are the only cases paying attention to the effect of internal flow pattern on the atomization. However, the results are restricted to simplified conditions and geometry, and water and air as working fluids.

A broad range of time and length scales are involved in atomization; thus, approximations and modeling of unresolved sub-grid scale phenomena become inevitable in CFD of such multiphase flow phenomena (Li, et al., 2020). The numerical simulation of the liquid spray generation often aims in predicting drop size distribution, spray penetration length and spray cone angle (Zhou, et al., 2019 a) and (Zhou, et al., 2019 b). Since the liquid spends most of its residence time in the form of droplets, simulation methodologies for the dispersed multiphase flow are usually utilized. The two widely

103   implemented approaches used for the description of the dispersed phase are the Eulerian-Eulerian

104   and Eulerian-Lagrangian.

105   The Eulerian-Eulerian multiphase approach describes the motion of the dispersed phase by the same

106   means as the continuous phase, i.e. a set of Navier-Stokes equations for the continuity and

107   momentum transport, potentially along with transport equations for energy and other conserved

108   quantities. The gas-liquid interface can be tracked by an additional transport equation such as the

109   widely used VOF method (Hirt & Nichlos, 1981) or similar and early applications to internal nozzle

110   flow and atomization (Arcoumanis, et al., 1999) and (Gavaises & Arcoumanis, 2001). Such methods

111   requires much smaller time steps and much higher mesh resolutions than diffuse interface

112   approaches and Eulerian-Lagrangian methods, as the computational mesh around the phase

113   boundary of each droplet must be refined enough to adequately resolve. The volume displacement is

114   inherently accounted for, which can be important for the dense part of the spray. However, this

115   method is prohibitive in terms of computational expenses and requires large HPC resources.

116   In Eulerian-Lagrangian multiphase approaches (Jiang, et al., 2010), referred to as Discrete Particle

117   Methods (DPM), the gas/carrier phase is still represented by solving the governing equation of the

118   flow but the liquid phase is represented by a number of discrete computational particles, which are

119   tracked through the domain by solving the particle's equation of motion. Particle tracker use physical

120   properties of individual droplets in order to account for the exchange of mass, momentum and

121   energy etc. with the continuous phase. This approach is relatively inexpensive since it allows the

122   mesh to be coarser than the size of the droplets. However, the gas volume displacement is usually

123   ignored; this may affect the solution's accuracy, hence these so-called dense models have been

124   developed (Tonini, et al., 2008). Furthermore, in the regions where spray does not consist of discrete

125   spherical droplets, special models must be employed to predict the primary breakup of the initial

126   contiguous jet.

127　ANSYS Fluent provides the capability to combine the above mentioned two approaches through VOF-

128　to-DPM transition mechanism. The initial jet and its primary breakup are predicted using VOF

129　formulations on sufficiently fine mesh, while the resulting dispersed part of the spray is predicted by

130　the DPM. The ELSA model (Vallet, et al., 2001) and (Nykteri, et al., 2020) is another alternative

131　approach that provides a dynamic transition between an Eulerian and a Lagrangian framework in the

132　primary and secondary liquid spray atomization regions, respectively. The hybrid VOF-to-DPM model

133　automatically finds the liquid lumps detached from the liquid core in the VOF solution. It then checks

134　for their eligibility for the VOF-to-DPM model transition against the user specified criteria of the lump

135　size and asphericity. If a liquid lump satisfies the criteria, the liquid lump is removed from VOF solver

136　and converted to a point mass in the Lagrangian formulations. Converting liquid lumps to Lagrangian

137　formulation does not impose volume displacement on the continuous phase VOF flow simulations. In

138　order to circumvent spurious momentum sources, a volume of a gas with the same volume as the

139　liquid lump is created in the VOF simulation to maintain the volume conservation. The hybrid VOF-to-

140　DPM model is validated against the experimental studies to determine the Sauter mean diameter

141　(SMD) drop size distribution for a liquid jet in air cross-flow (Schtze, et al., 2018) and (Sami, et al.,

142　2019) and also the reverse transition mechanism i.e. DPM-to-VOF is reported to agree well with the

143　experimental studies to determine the film formation from the drops (Kumar, et al., 2018).

144　In the present study, the multiphase flow through the internally mixing twin-fluid Y-jet atomizer is

145　numerically modelled to determine the internal flow behavior and the subsequent atomization

146　mechanism. It is the first numerical study to report the atomization mechanism of the internally

147　mixing twin-fluid Y-jet atomizer. The influence of two dimensionless operating parameters, namely

148　gas-to-liquid mass flow rate ratio and liquid-to-gas momentum ratio are compared; the latter is

149　found to be more appropriate dimensionless parameter to describe the internal flow behavior and

150　the atomization characteristics, as it defines to a large extend the liquid and gas distribution inside

151　the atomizer, which then affects the near-nozzle atomization and the distribution of the formed

152　ligaments and droplets. It should be also mentioned that although more sophisticated atomization

153   models exist in the literature for the fragmentation of liquids, the applied model has been validated

154   from the author's group for other flow conditions, like for example the secondary break-up of liquid

155   droplets (Stefanitsis, et al., 2019a), (Stefanitsis, et al., 2019b), (Strotos, et al., 2018), (Strotos, et al.,

156   2016a), (Strotos, et al., 2016b) and (Strotos, et al., 2011). For the specific conditions simulated here,

157   the complexity of the flow within the atomizer, it is unfortunate that quantitative experimental data

158   for the atomizing spray that would be needed for quantitative validation of the applied

159   computational models do not exist.

160   Following, the computational model utilized and the geometry and operating conditions are

161   described, followed by the presentation of the results; these include initially the flow structure inside

162   the atomizer and then its influence on the spray formation; the most important conclusions are

163   summarized at the end.

164 Numerical Method

165   VOF

166   The compressible Navier-Stokes equations are numerically solved using the finite volume

167   approximation; the Volume of Fluid (VOF) technique with Geometric Reconstruction Scheme is

168   employed in ANSYS Fluent with a time step of 10^{-8} to model the gas-liquid interface. The interface is

169   modeled as interpenetrating media; the two phases are sharing same properties while the bulk

170   properties of the individual phase are scaled according to the cell's volume fraction which varies

171   between zero and one.

172   The corresponding transport equations that consider the volume fraction in the cell, with ρ_q

173   representing the density and $\overrightarrow{V_q}$ the velocity vector of the qth phase, are:

$$\frac{d}{dt}\left(\alpha_q \rho_q\right) + \nabla.\left(\alpha_q \rho_q \overrightarrow{V_q}\right) = 0 \tag{1}$$

174   The single set of momentum equation is shared among the phases based on mixture properties.

$$\frac{d}{dt}(\rho\vec{V}) + \nabla.(\rho\vec{V}\vec{V}) = -\nabla P + \nabla.\left[\mu(\nabla\vec{V} + \nabla\vec{V}^T)\right] + \rho\vec{g} + \vec{T}_\sigma \tag{2}$$

175

176   Where density is defined as: $\rho = \sum \alpha_q\rho_q$, viscosity as: $\mu = \sum \mu_q\alpha_q$, and velocity as: $\vec{V} =$

177    $\frac{1}{\rho}\sum_{q=1}^{n} \alpha_q\rho_q\vec{V}_q$ $\vec{T}_\sigma$ is the volumetric force source term arising due to the surface tension. It is

178   modelled by continuum surface force model proposed by Brackbill et al. (Brackbill, et al., 1992). This

179   model treats the surface tension as the pressure jump across the interface. The forces at the surface

180   are expressed as volume forces using the divergence theorem:

$$T_\sigma = \sum_{pairs,p,q} \sigma_{p,q} \frac{\alpha_p\rho_p k_q\nabla\alpha_q + \alpha_q\rho_q k_p\nabla\alpha_p}{\frac{1}{2}(\rho_p + \rho_q)} \tag{3}$$

181

182   The curvature of one surface is negative of other, $k_p = -k_q$ and divergence of the volume fraction is

183   negative of other $\nabla\alpha_p = -\nabla\alpha_q$. This simplifies the equation to:

$$T_\sigma = \sigma_{p,q} \frac{\rho k_p\nabla\alpha_p}{\frac{1}{2}(\rho_p + \rho_q)} \tag{4}$$

184   The total energy of the flow is modelled by following equation.

$$\frac{d}{dt}(\rho E) + \nabla.\left(\vec{V}(\rho E + P)\right) = \nabla.\left(K_{eff}\nabla T + \bar{\bar{\tau}} \cdot \vec{V}\right) \tag{5}$$

185

186   Here K_{eff} is effective thermal conductivity, $\bar{\bar{\tau}}$ is the viscous stress tensor; the energy E and

187   temperature T are mass averaged variables.

$$E = \frac{\sum_{q=1}^{n} \alpha_q\rho_q E_q}{\sum_{q=1}^{n} \alpha_q\rho_q} \tag{6}$$

188

189   E_q is the internal energy of each phase; both phases share the same temperature.

190   Transition

191   Asphericity is the shape base criterion used by VOF-to-DPM model to identify the liquid lumps which

192   can be converted from resolved liquid using VOF model to particles tracked with the DPM model. Its

193   value is zero for a perfect sphere. Asphericity values of the liquid lumps are determined in two ways,

194   namely calculated from normalized radius standard deviation and radius-surface orthogonality. In

195   the first method, for every facet of the liquid lump surface, the distance between the facet center

196   and the lump center of gravity is calculated and then normalized by the average radius. In the second

197   method, for every facet of the liquid lump surface, a vector from the lump's center of gravity to the

198   center of the lump boundary facet is computed and then used in a dot product with the facet unit

199   normal vector. Only lumps for which the asphericity values calculated from both methods are below

200   the user-specified maximum asphericity values are selected for transition from VOF liquid to DPM

201   particles.

202   DPM

203   The trajectory of the discrete phase is predicted by integrating the force balance on the particle. The

204   force balance equation, which is written in a Lagrangian reference frame, equates the particle inertia

205   with the force acting on the particle. It can be written as:

$$\frac{d\vec{V}_{pr}}{dt} = F_D\left(\vec{V} - \vec{V}_{pr}\right) + \frac{\vec{g}(\rho_g - \rho)}{\rho_{pr}} \tag{7}$$

206   Where $F_D\left(\vec{V} - \vec{V}_{pr}\right) + \frac{\vec{g}(\rho_{pr} - \rho)}{\rho_{pr}}$ is the drag force per unit particle mass and

$$F_D = \frac{18\mu}{\rho_{pr}d_{pr}^2} \frac{C_D Re_r}{24} \tag{8}$$

207   Here, $\vec{V}$ is the fluid phase velocity, $\vec{V}_{pr}$ is the particle velocity, μ is the molecular viscosity of the fluid,

208   ρ_{pr} is the density and d_{pr} is the diameter of the particle. Re_r is the relative Reynolds number, it is

209   defined as:

$$Re_r = \frac{\rho d_p |\vec{V}_{pr} - \vec{V}|}{\mu} \tag{9}$$

210   C_D is the drag coefficient; according to Morsi and Alexander model (Morsi & Alexander, 1972), it is

211   defined as:

$$C_D = a_1 + \frac{a_2}{Re} + \frac{a_3}{Re^2} \tag{10}$$

212   Where a_1, a_2 and a_3 are defined as:

$$a_1, a_2, a_3 = \begin{cases} 0, 24, 0 & 0 < Re < 0.1 \\ 3.690, 22.73, 0.0903 & 0.1 < Re < 1 \\ 1.222, 29.1667, -3.8889 & 1 < Re < 10 \\ 0.6167, 46.50, -116.67 & 10 < Re < 100 \\ 0.3644, 98.33, -2778 & 100 < Re < 1000 \\ 0.357, 148.62, -47500 & 1000 < Re < 5000 \\ 0.46, -490.546, 578700 & 5000 < Re < 10000 \\ 0.5191, -1662.5, 5416700 & Re > 10000 \end{cases} \tag{11}$$

213

214   The heat balance to relate particle temperature to convective heat transfer at the droplet/particle

215   surface is modeled by following equation:

$$m_{pr} c_{pr} \frac{dT_{pr}}{dt} = hAr_{pr}(T_\infty - T_{pr}) \tag{12}$$

216   where m_{pr} is the mass of the particle, c_{pr} is the heat capacity of the particle, Ar_{rp} is the surface area

217   of the particle, T_∞ is the local temperature of the continuous phase and h is the convective heat

218   transfer coefficient. The convective heat transfer coefficient is evaluated using the correlation of

219   Ranz and Masrshall (Ranz & Marshall, 1952 a) and (Ranz & Marshall, 1952 b) as:

$$\frac{hd_p}{k_\infty} = 2.0 + 0.6Re_r^{1/2} Pr^{1/3} \tag{13}$$

220   Here k_∞ is the thermal conductivity and $Pr\left(c_p\mu/k_\infty\right)$ is the Prandtl number of the continuous

221   phase

222   Turbulence Modeling

223   Scale resolving technique is adopted to resolve larger eddies through Wall Modeled LES (WMLES)

224   Model. As Reynolds number increases and the boundary layer become thinner, the size of important

225   energy bearing eddies decreases. In Large Eddy Simulations (LES), the important energy bearing

226   eddies must be resolved, thus the cost of maintaining grid resolution becomes prohibitive while

227   much smaller time steps are also required. A promising approach to overcome the Reynolds number

228   scaling limitation of LES is the algebraic Wall-Modeled LES approach. In this model larger eddies are

229   resolved while eddies in thinner near-wall regions; in which the wall distance is much smaller than

230   the boundary-layer thickness but it is still potentially very large in wall units (Piomelli & Balaras,

231   2002), is modeled with RANS, hence considerably reducing the computational cost. Gaussian filter is

232   applied to filter out eddies based on the length scale Δ (Shur, et al., 2008).

$$\overline{\emptyset}(x,t) = \int_D \emptyset(x',t)G(x,x',\Delta)dx' \tag{14}$$

$$\Delta = min(max(C_w.ds_w; C_w.h_{max}, h_{wn}); h_{max}) \tag{15}$$

233   h_{max}= maximum edge length, h_{wn}= grid step in wall-normal direction, C_w=0.15, d_w= distance from

234   wall.

235   After putting the filtered out variables in Navier-Stokes equation and rearranging the terms, it could

236   be expressed as:

$$\frac{(\partial \overline{V}_i)}{\partial t} + \frac{\partial(p\overline{V}_i\overline{V}_j)}{\partial x_j} = -\frac{\partial \overline{P}}{\partial x_i} + \frac{\partial(\tau_{ij} + \tau_{ij}^S)}{\partial x_j} \tag{16}$$

237   This equation could be resolved except of the subgrid-scale stress τ_{ij}^S. It can be expressed by the

238   Boussinesq hypothesis (Hinze, 1975) as:

$$\tau_{ij}^S - \frac{1}{3}\tau_{kk}\delta_{ij} = -2\mu_t S_{ij} \tag{17}$$

239   The subgrid scale eddy viscosity is modeled with the Smagorinsky SGS model (Smagorinsky, 1963),

240   the van Driest damping (Van Driest, 1956) and mixing length model as:

$$v_t = min\left[(kds_w)^2, (C_{smag}\Delta)^2\right][1 - exp[-(y^+/25)^3]]|S - \Omega| \tag{18}$$

241    $C_{smag} = 0.2$ is the Smagorinsky constant, as established by Shur et al (Shur, et al., 1999), $\Omega=$ is the

242   vorticity, S is the magnitude of the strain tensor, k $= 0.41$ is the Von Karman Constant.

243 Test Case Simulated

244 Figure 2 depicts the geometry used in the simulations. The figure is not drawn according to scale. The

245 working fluids are superheated steam and light fuel oil. The liquid port has diameter (d_l) 2.1 mm and

246 length (l_l) 30 mm. The gas port has diameter (d_g) $1.6\ mm$ and length (l_g) $4\ mm$. Both the mixing

247 port and the premixed zone has diameter $2.6\ mm$ and lengths $12.4\ mm$ and $5.6\ mm$ respectively.

248 The angle between the fuel port and the mixing port is $42.5°$. The pressure and temperature

249 conditions at the inlet of the fuel port are $20°C$ and 19 bars, and at the inlet of steam port are $210\ °C$

250 and 11 bars respectively. The density and kinematic viscosity of the light fuel oil are $0.93\ kg/m^3$ and

251 $4,1\ mm^2/s$ respectively, while steam is modeled as ideal gas. The condition at the outlet of

252 simulation zone is air at 1 bar and room temperature. The Sauter mean diameters (SMD) of the

253 droplets are measured on each 3 mm slot on the plane A along the Y axis as shown in Figure 2. Plane

254 A is located at the distance of 32 mm from the nozzle orifice. This distance is chosen on the basis of

255 computational affordability. The geometry is meshed in ANSYS Meshing with polyhedral grid.

256 Dynamic solution-adaptive mesh refinement in ANSYS Fluent is used to dynamically adapt the mesh

257 at the gas-liquid interface in the VOF simulations through polyhedral unstructured mesh adaption

258 (PUMA) method. This adaptation travels with the gas-liquid interface and the number of the cells

259 changes with the flow, once liquid lumps are converted into the DPM particles; coarser grid is used to

260 track the particles. This method significantly reduces the mesh count. Three levels of dynamic mesh

261 refinement are used while the minimum cell volume is set to the order of $10^{-16}\ m^3$. The minimum

262 cell volume is chosen based on the droplet size distribution to avoid over-refinement of the grid in

263 order to run the simulations more efficiently. A grid independent study is conducted with a minimum

264 cell volume of $10^{-16}\ m^3$ and $10^{-17}\ m^3$ (equivalent cubic cell size of ~ 5 and $\sim 3\mu m$, respectively).

265 The results are displayed in the appendix I (Figure 9 and Figure 10). It can be seen in Figure 9 that the

266 drop size distribution and in Figure 10 that the average volume fraction of the light fuel oil over one

267 hundred thousand time steps are almost the same for both meshes. Figure 3 shows an instantaneous

268   picture of numerical grid; it can be seen that the mesh is refined around gas-liquid interface. Mass

269   flow inlet boundary conditions are used for the inlets and pressure outlet boundary condition is used

270   for the outlet. In the first set of the simulations the mass flow rate of the steam is kept constant at

271    $0.00400\ kg/s$ while the mass flow rate of fuel oil is varied from $0.1329\ kg/s$ to $.38\ kg/s$; the

272   corresponding values of steam-to-fuel oil mass flow rate ratios are from 0.01053 to 0.0301

273   respectively. In the second set of simulations, the mass flow rate of the steam is kept constant at

274    $0.0005\ kg/s$ while the mass flow rate of the fuel oil is varied from $0.005\ kg/s$ to $0.0167\ kg/s$; the

275   corresponding steam-to-fuel oil mass flow rate ratios are from 0.03 to 0.1 respectively. The Reynold

276   numbers for the flow conditions simulated are between 10,000 and 13,000. They are calculated from

277   the following expression:

$$Re = \frac{\rho_{mix,M} V_r d_m}{\mu} \tag{19}$$

278   Here $\rho_{mix,M}$ is the average mixture density of the gas and liquid at the mixing point, V_r is the relative

279   velocity between gas and liquid phase, and d_m is the mixing port diameter.

280   The asphericity value for the VOF-to-DPM transition mechanism is initially set to the value of 0.01. As

281   the flow is developed in the mixing port of the atomizer, it is changed to the value of 2.5 to track the
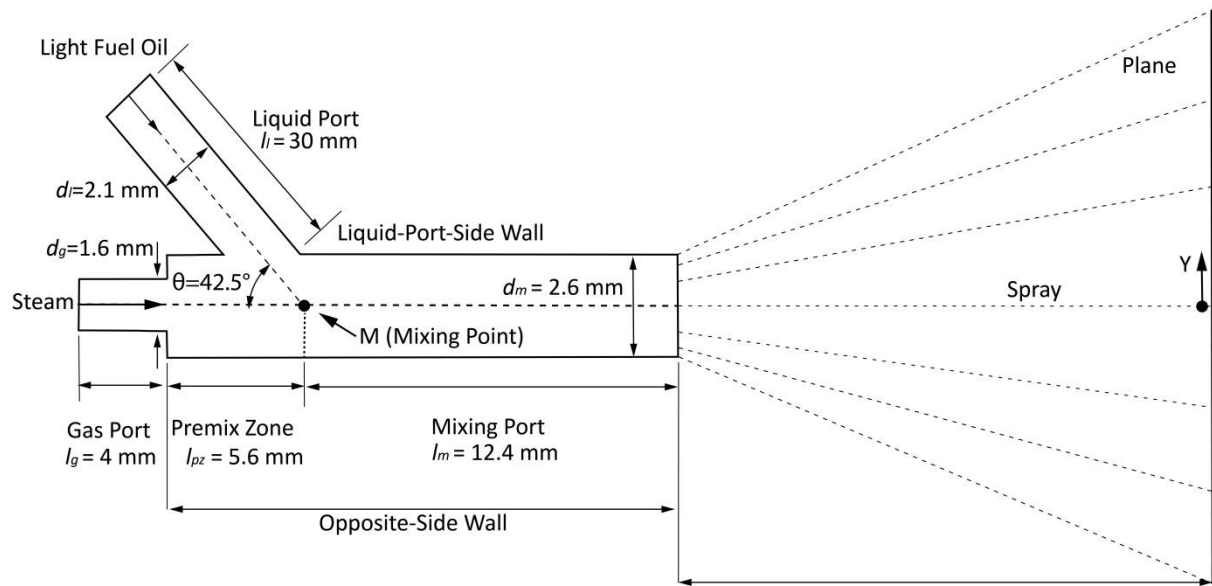
282   droplets and measure its SMD.

283

284   Figure 2: Geometry of twin-fluid Y-jet atomizer used in the simulation and schematic explanation of the subsequent spray
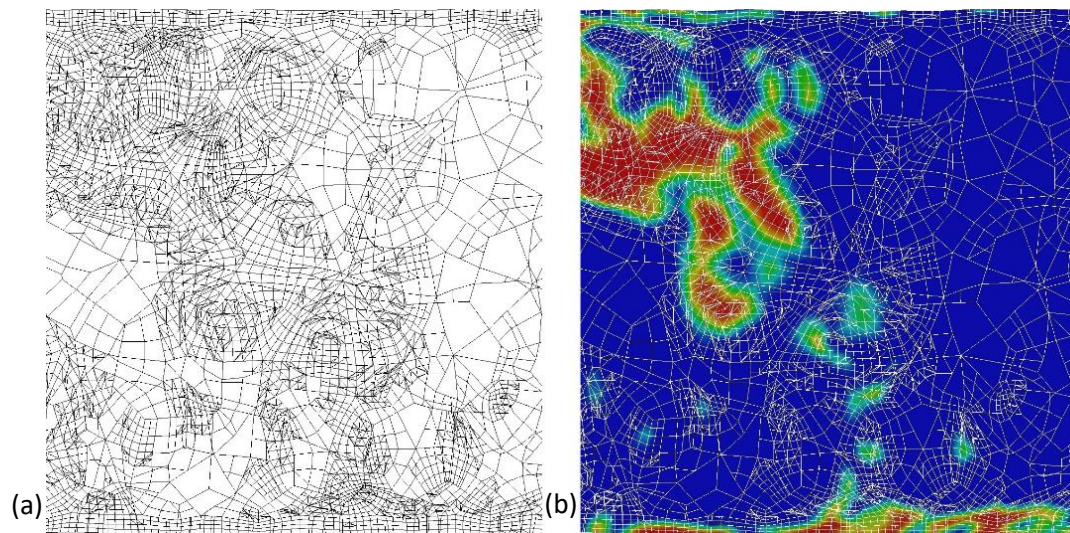285   formation.

286

287

288

289

290

291   (a)   (b)

292

       Figure 3 (a) Instantaneous grid (b) Instantaneous grid with super imposed volume fraction of light fuel oil.
293
294
295

Results & Discussion

297   Visualization of the simulation results has been carried out to analyze the internal flow behavior

298   within the mixing-port of the twin-fluid Y-jet atomizer. Figure 4 show the internal flow patterns

299   within the mixing-port of atomizer for two different steam mass flow rates and various oil mass flow

300   rates. For a reference, a schematic of the mixing-port at the same scale is drawn at the top of Figure

301   3. The red colour depicts the volume fraction of fuel oil to be 1 while blue colour depicts the volume

302 fraction of the fuel oil to be zero i.e. the volume fraction of the steam as 1. The instability of the

303 liquid jet emanating from the liquid port into the mixing port is amplified by the impingement of high

304 velocity gas stream; leading to the creation of smaller liquid ligaments and sheets. This phenomenon

305 could be explained by the shear action of the gas stream and by the wave lengths that grow on the

306 surface of the liquid jet/column, which are affected by surface tension, aerodynamic and viscous

307 forces (Dombrowski & Johns, 1963). The high relative velocity of the gas helps the dispersion of the

308 liquid and delays or minimise the chances of droplet coalescence (Pacifico & Yanagihara, 2014).

309 At first, it can be realized from the contours in the Figure 4 that both M_l and M_g clearly influence the

310 oil film formation within the mixing port. The amount of oil stream crossing the mixing port increases

311 with a decrease of M_g and/or an increase of M_l, and forms a thicker oil film at the opposite side wall.

312 The internal flow pattern far downstream of the mixing point becomes an annular-mist flow with

313 asymmetrical film thickness along the wall of the mixing-port, as characterized by Mullinger and

314 Chigier (Mullinger & Chigier, 1974), Andreussi et al. (Andreussi, et al., 1994), (Andreussi, et al., 1992),

315 Pacifico and Yanagihara (Pacifico & Yanagihara, 2014) Mlkvik et al. (Mlkvik, et al., 2015) and Nazeer

316 et al. (Nazeer, et al., 2019). The rate of direct drop formation within the mixing port is also strongly

317 dependent on both M_g and M_l. That is, the number of drop increases with an increase in M_l and/or

318 M_g (Song & Lee, 1996).

319 On the same figure, the values of the gas-to-liquid mass flow rate ratio (M_g/M_l) and the liquid-to-gas

320 momentum ratio (φ) are also shown. These parameters are already adopted in the studies (Neya, et

321 al., 1975), (De Michele, et al., 1991), (Andreussi, et al., 1992), (Song & Lee, 1994), (Andreussi, et al.,

322 1994), (Pacifico & Yanagihara, 2014), (Mlkvik, et al., 2015) and (Nazeer, et al., 2019). Here φ is

323 defined as:

$$\varphi = \frac{G_l^2 d_l^2 \rho_{gM}}{G_g^2 d_m^2 \rho_l} \sin\theta \qquad (20)$$

324   Where "G" is the mass velocity, "ρ" is the density, "d_m" is the mixing port diameter and "θ" is the

325   angle between liquid and gas ports. The indices "g" and "l" denote the gas and liquid respectively;

326   ρ_{gM} is the density of the steam at the mixing point.

327   From Figure 4 one can point out that when the gas flow rates are different while M_g/M_l is kept

328   constant (see Figures 4a and 4i), the flow pattern appears to be much different. In fact, when

329   momentum ratios are near to each other, for instance (4a and 4f) and (4h and 4c) flow development

330   looks very similar. Thus, from the above observations, the liquid-to-gas momentum ratio (φ) seems

331   to be a better dimensionless parameter to explain the internal flow pattern than the gas-to-liquid

332   mass flow rate ratio. Song and Lee (Song & Lee, 1996) also reached to the conclusion that

333   momentum ratio is a better parameter to describe the internal flow pattern.

334   Figure 5 helps to explain the variation in gas and liquid flow patterns within the mixing port of Y-jet

335   nozzle based on the momentum ratio. The contours of the volume fraction of light fuel oil are

336   displayed for the liquid-to-gas momentum ratios of 3.2, 7.3 and 9.4. When the liquid-to-gas

337   momentum ratio is low (say $\varphi < 7$, Figures 4a, 4e, 4f and 4g), most of the liquid forms thick film at

338   liquid-port-side wall of the mixing port. This is because the gas jet momentum dominates and liquid

339   stream cannot penetrate into the mixing-port easily. Due to this, the main stream of the gas tends to

340   be deflected towards the opposite side wall by the liquid film and thus, a large recirculation appears

341   in the premix zone. Hence, a portion of the liquid stream flows in a film shape toward the upstream

342   by recirculating gas. For example the liquid film in the upper left corner of Figures 4b, 4f, 4g and 4i

343   clearly indicates the reverse flow of the liquid film by strong recirculation of the gas. As the main gas

344   stream at the exit of the gas port meets the reverse flow, it disintegrates in to small droplets and

345   flows downstream along the core, as it can be seen in Figure 6. At the same time, as it can be seen in

346   Figures 4a, 4e, 4f and 4g, droplets are also entrained from the main liquid film, flowing downstream.
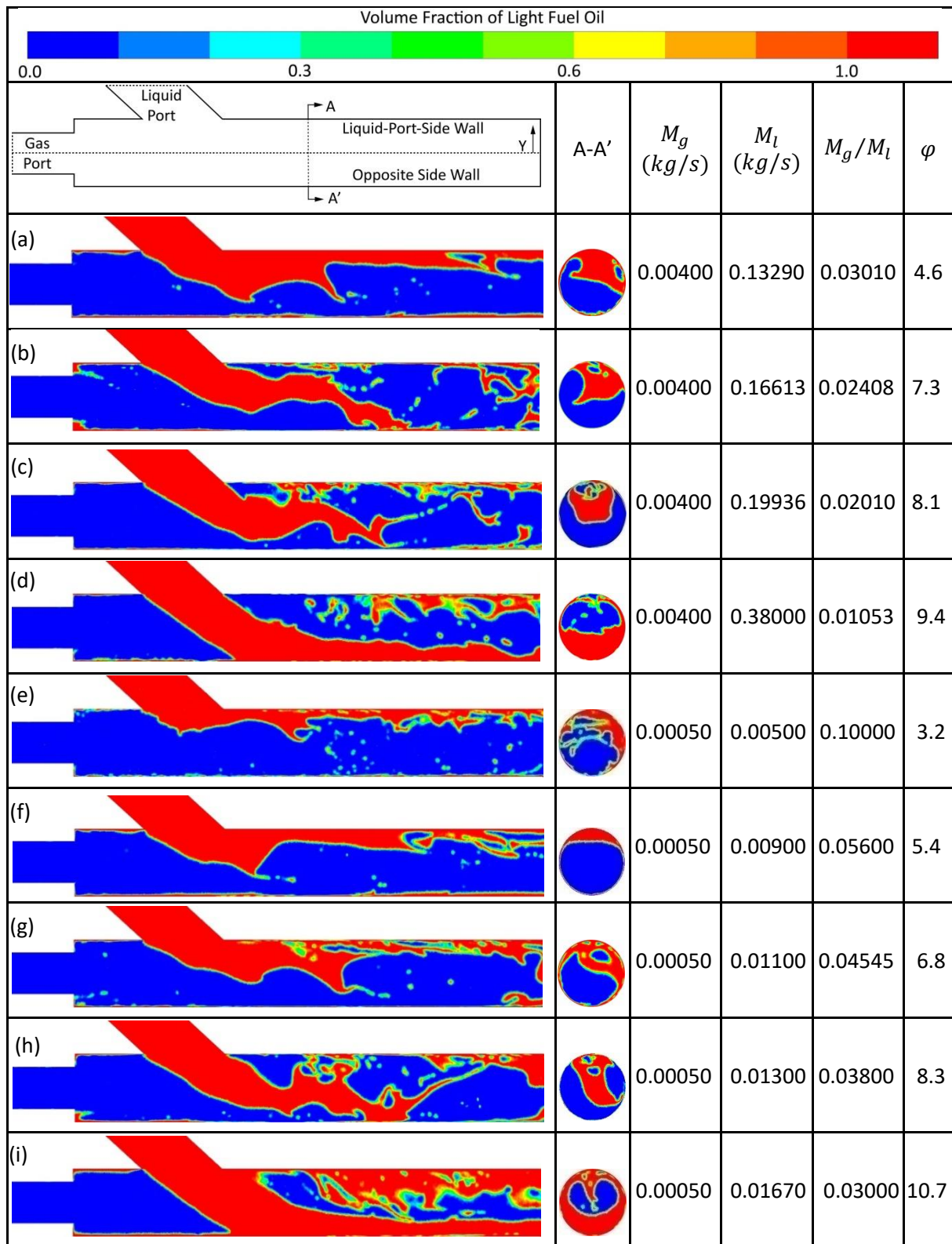
347

Figure 4 Internal flow pattern within the mixing port of internally mixing twin-fluid Y-jet atomizer at the flow time of 0.001 s for the liquid-to-gas momentum ratios of (a) 4.6, (b) 7.3, (c) 8.1, (d) 9.4, (e) 3.2, (f) 5.4, (g) 6.8, (h) 8.3 and (i) 10.7.
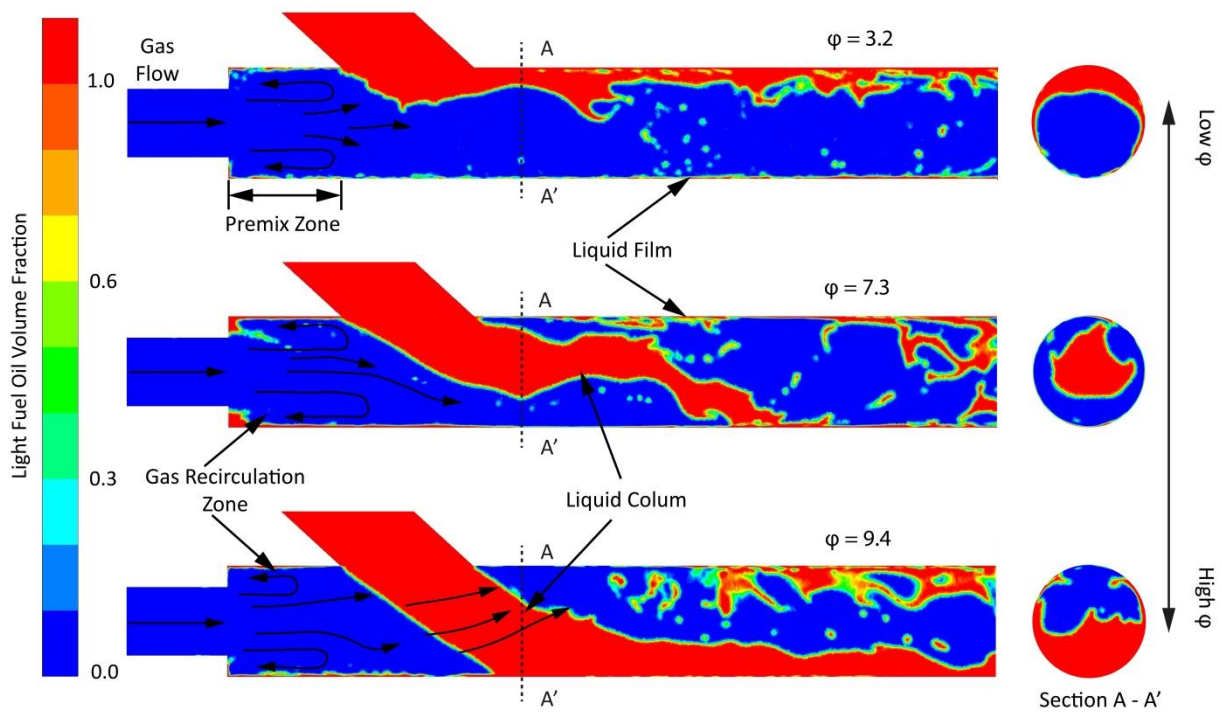
349

350

Figure 5 Illustration of internal flow pattern based on liquid-to-gas momentum ratio.

352

When the liquid-to-gas momentum ratio increases (for $7 < \varphi < 9$, Figures 4b, 4c and 4h), the liquid jet penetrates into the center of the mixing port and starts to blocking the path of the flowing gas ensuing from the gas port; this leads to deflection of the gas stream towards the opposite side wall. This is denoted as blockage effect (Mullinger & Chigier, 1974). Thus, a substantial amount of liquid film at the opposite side is entrained into the gas core by the highly deflected gas stream while the rate of the entertainment increases with the amount of gas stream deflection. The number of droplets formed around the mixing point from the liquid column increases with increasing penetration depth of liquid, since the interfacial area between the gas and liquid increases. The liquid jet in this regime is unstable and gradually breaks up as a result of imbalance between surface forces, velocity fluctuations, pressure fluctuations and steep velocity gradients. This leads to temporally fluctuating liquid sheet/film formation within in the mixing-port, just before the orifice exit (Figures 4b and 4h).

365   As the liquid-to-gas momentum ratio increases further ($\varphi > 9$, Figures 4d and 4i), part of the liquid

366   jet reaches the opposite wall and the liquid film thickness at both sides of the mixing port becomes

367   similar in thickness. If the liquid-to-gas momentum ratio increases further, the liquid jet completely

368   reaches the opposite side wall and the film thickness at the opposite side wall becomes thicker than

369   the liquid-port-side wall, as can be seen in the Figure 4d. With this condition, the blockage effect

370   becomes more prominent because the gas stream has to flow around the liquid jet crossing the

371   mixing point. Due to the high shear of the gas flow, thin sheets of the liquid are extracted from the

372   liquid jet around the mixing point (liquid-port-side wall Figures 4d and 4i). These sheets are further
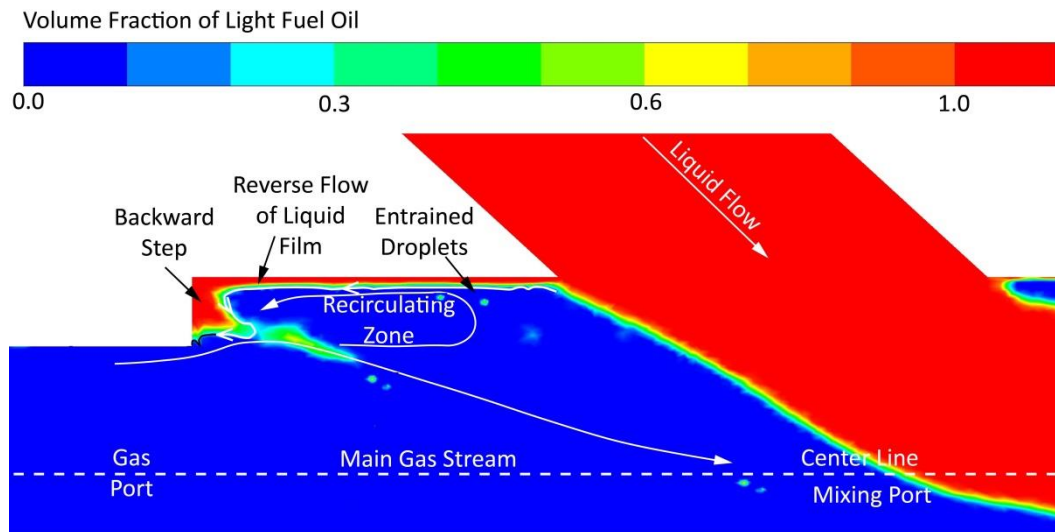

Figure 6 Illustration of the recirculating flow in the premix zone of the mixing port of the atomizer.

373   broken down into smaller droplets in the downstream flow. The quantity of these liquid sheet

374   formations increases with the deeper penetration of the liquid jet or with greater gas flow rate.
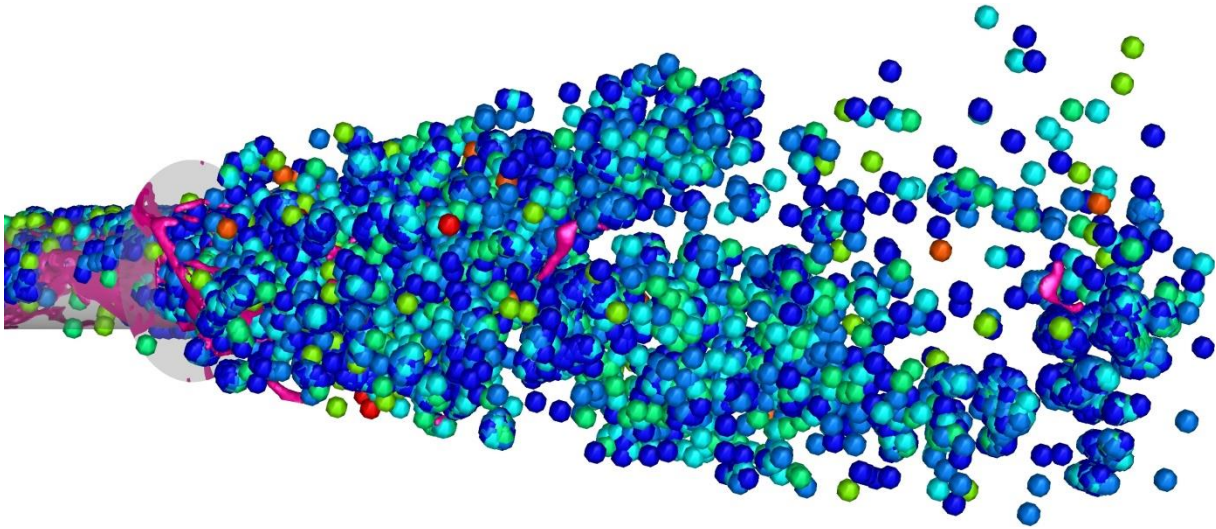
375

376

377

Figure 7 Spray formation by internally mixing twin-fluid Y-jet atomizer at the flow time of 0.0006 s for the liquid-to-gas momentum ratio of 7.3. The magenta colored blobs and ligaments represent the liquid resolved by VOF formulations and spherical particle represents the liquid droplets tracked by DPM model.

378 Figure 7 shows the spray formation process of internally mixing twin-fluid Y-jet atomizer. The

379 magenta colored blobs and ligaments depict the resolved liquid by the VOF method. Once the

380 specified criteria of aspherecity are satisfied, the resolved liquid is turned into discrete droplets, as

381 represented by the spherical particles in Figure 7. Figure 8 shows the Sauter Mean Diameter (SMD)

382 drop size distribution for various liquid-to-gas momentum ratios measured on the plane A along the

383 Y axis as indicated in Figure 2. The droplet size distribution is strongly affected by the internal flow

384 pattern and the initial atomization within the mixing port of the nozzle, as explained earlier. That is,

385 the small droplets at the center are forming from the core flow within the mixing port of the

386 atomizer, whereas the larger droplets at both sides are forming from the annular liquid film present

387 on the walls of the mixing port. It can be also noticed that as the momentum ratio increases, the

388 peak value of the Sauter Mean Diameter in the positive Y axis decreases, indicating that the liquid

389 film thickness at the liquid-port-side wall of the mixing port decreases, due to easier penetration of

390 the liquid column into the gas stream. When the momentum ratio is less than 5.4 (Figures 8a, 8b and

391 8c), the values of SMD in the negative Y axis changes slightly with the increasing momentum ratios.

392 This is because the liquid column does not have enough momentum to reach the opposite side wall.

393 However, as the liquid-to-gas momentum ratio increases further than that, the values of SMD in the

394   negative Y axis become sufficiently large and the distribution becomes somewhat symmetrical

395   (Figure 8d). If φ increases further, the momentum of the liquid column dominates and hence the

396   values of SMD in the negative Y axis become larger than the values in positive Y axis; the curve again

397   shows asymmetrical shapes. At extremely high values of momentum ratio (Figure 8h), a sudden

398   decrease in the values of SMD in the positive Y axis is observed. This is due to the shear-induced

399   breakup caused by the increased blockage effect (Figure 4h). These distributions agree well with the

400   film thickness variation within the mixing port measured by Andreussi et al. (Andreussi, et al., 1994)

401   and the drop size distribution measured by (Song & Lee, 1996).

402

403

404

405

406

407

408

409

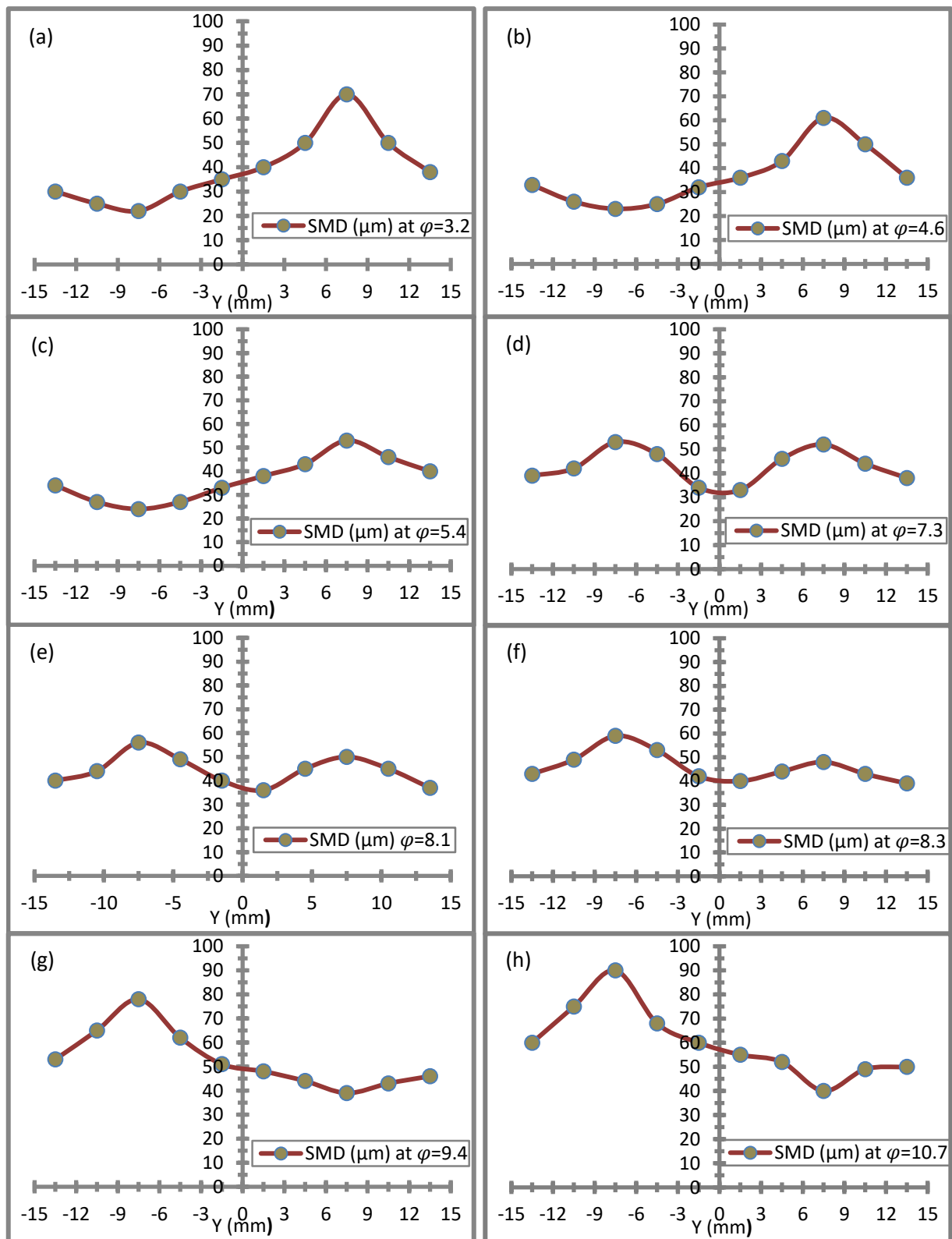410

411

412

413

414

415

416

417

418

419

Figure 8 Sauter mean diameter drop size distribution for the liquid-to-gas momentum ratios of (a) 3.2, (b) 4.6, (c) 5.4, (d) 7.3, (e) 8.1, (f) 8.3, (g) 9.4 and (h) 10.7.

Conclusion

Simulation results have been presented for the internal flow behavior and the atomization mechanism of internally mixing twin-fluid Y-jet atomizers. Working fluids were super-heated steam and light fuel oil. The multiphase flow was modeled by hybrid Eulerian-Eulerian and Eulerian-Lagrangian approach through VOF-to-DPM transition mechanism. Adaptive mesh refinement was used to resolve the gas-liquid interface on the fine mesh required by the VOF formulations. When the criteria of asphericity were satisfied, discrete droplets were tracked on the coarser mesh through DPM model. A hybrid RANS and LES technique, i.e. WMLES (wall modeled large eddy simulations) was used to resolve the larger eddies with LES formulations, while smaller eddies were modeled with the Prandtl length model. Two dimensionless parameters namely, gas-to-liquid mass flow rate ratio and the liquid-to-gas momentum ratio have been investigated; the latter is considered to be a more representative dimensionless parameter to describe the internal flow behavior and spray characteristics. The variation in the internal flow pattern, characterized by the penetration of the liquid column into the gas core and the film flow within the mixing port could be effectively explained by the liquid-to-gas momentum ratio. The simulations have confirmed that variation in the circumferential liquid film thickness within the mixing port coincides well with the spatial distribution of the droplets outside the atomizer. Moreover, the variation in the droplet SMD distribution over the Y direction as the function of the liquid-to-gas momentum ratio, agrees well with the mean film thickness and drop size distribution reported previously in the open literature, except for the sharp decrease in the SMD in the positive Y direction at extremely high liquid-to-gas momentum ratios.

Data Availability Statement

ANSYS Fluent case and data files of the simulations that support the findings of this study are available from the corresponding author upon reasonable request.

Acknowledgements

460   # References

461   Andreussi, P. et al., 1994. *Measurement of Film Thickness within a Y-Jet Atomizer.* s.l., International
462   conference on liquid atomization and spray systems, pp. 632-639.

463   Andreussi, P., Tognotti, L., Michele, G. D. & Graziadio, M., 1992. Design and Characterization of Twin-
464   Fluid Y-Jet Atomizers. *Atomization and Sprays,* Volume 2, pp. 45-59.

465   Arcoumanis, C., Gavaises, M., Argueyrolles, B. & Galzin, F., 1999. Modeling of Pressure-Swirl
466   Atomizers for GDI Engines. *Transactions Journal of Engines, SAE Paper,* 108(3), pp. 516-532.

467   Barreras, F., Lozano, A., Ferreira, G. & Lincheta, 2008. *The effect on the inner flow on the performance*
468   *of a twin-fluid nozzle with an iternal mixing chamber.* Como Lake, European Conference on Liquid
469   Atomization and Spray Systems.

470   Barreras, F., Lozano, A., Ferreira, G. & Lincheta, E., 2006. *Study of the Internal Flow Condition on the*
471   *Behavior of Twin-Fluid Nozzle with Internal Mixing Chamber.* Kyoto, International Conference on
472   Liquid Atomization and Spray Systems.

473   Brackbill, J. U., Kothe, D. B. & Zemach, C., 1992. A continuum method for modeling surface tension..
474   *Journal of Computational Physics,* 100(2), pp. 335-354.

475   Buckner, H. N., Sojka, P. E. & Lefebvre, A. H., 1990a. Effervescent atomization of coal-water slurries.
476   *ASME publication,* Volume 30, pp. 105-108.

477   Buckner, H. N., Sojka, P. E. & Lefebvre, A. H., 1990b. *Effervescent atomization of non-Newtonian*
478   *single phase liquid.* Hartford, Connecticut, Proceedings of the fourth Annual Conference on
479   Atomization and Sprays.

480   De Michele, G., Graziadio, M., Morelli, F. & Novelli, G., 1991. *Characterization of the spray structure*
481   *of a large scale H.F.O. Atomizer.* Gaithersburg, Proceedings of ICLASS.

482   Dombrowski, N. & Johns, W. R., 1963. The aerodynamic instability and disintegration of viscous liquid
483   sheets. *Chemical Engineering Science,* 18(3), pp. 203-214.

484   Gavaises, M. & Arcoumanis, C., 2001. Modelling of sprays from high-pressure swirl atomizers.
485   *International Journal of Engine Reserach,* 2(2), pp. 95-117.

486   Hinze, J. O., 1975. *Turbulence.* New York: McGraw-Hill Publishing Co..

487   Hirt, C. W. & Nichlos, B. D., 1981. Volume of fluid (VOF) method for the dynamics of free boundaries.
488   *Journal of Computational Physics,* 39(1), pp. 201-225.

489   Inamura, T. et al., 2019. Effects of prefilmer edge thickness on spray characteristics in prefilming
490   airblast atomization. *International Journal of Multiphase Flow,* Volume 121.

491   Jiang, X., Siamas, G. A., Jagus, K. & Karayiannis, T. G., 2010. Physical modelling and advanced
492   simulations of gas-liquid two-phase jet flows in atomization and sprays. *Progress in Energy and*
493   *Combustion Science,* Volume 36, pp. 131-167.

494 Kufferath, A., Wende, B. & Leuckel, W., 1999. Influence of liquid flow condtions on spray
495 characteristics of internal-mixing twin-fluid atomizers. *International journal of heat and fluid flow,*
496 Volume 20, pp. 513-519.

497 Kumar, V. et al., 2018. *A hybrid approach for modeling fully resolved liquid film formation by*
498 *converting lagrangian particles to eulerian VOF structures.* Chicago, International Conference on
499 Liquid Atomization and Sprays Systems.

500 Lefebrve, A. H., 1992. Twin-Fluid Atomization: Factors Influencing Mean Drop Size. *Atomization and*
501 *Sprays,* Volume 2, pp. 101-119.

502 Lefebvre, A. H., 1980. Airblast Atomization. *Progress in Energy and Combustion Sciences ,* Volume 6,
503 pp. 223-261.

504 Li, H., Rutland, C. J., Perez, F. E. H. & Im, G. H., 2020. Large-eddy spray simulation under direct-
505 injection spark-ignition engine-like conditions with an integrated atomization/breakup model.
506 *International Journal of Engine Research.*

507 Li, Z. et al., 2012. Mixing and atomization characteristics in an internal-mixing twin-fluid atomizer.
508 *Fuel,* Volume 97, pp. 306-314.

509 Mlkvik, M. et al., 2015. Twin-Fluid atomization of viscous liquids: The Effect of atomizer construction
510 on breakup process, spray stability and droplet size. *International Journal of Multiphase,* Volume 77,
511 pp. 19-32.

512 Morsi, S. A. & Alexander, A. J., 1972. An investigation of Particle Trajectories in Two-Phase Flow
513 Systems. *Journal of Fluid Mechanics,* 55(2), pp. 193-208.

514 Mullinger, P. & Chigier, N., 1974. The Design and Performance of Internal Mixing Multijet Twin Fluid
515 Atomizers. *Journal of the institute fuel,* Volume 47, pp. 251-261.

516 Nazeer, Y. H., Ehmann, M., Koukouvinis, P. & Gavaises, M., 2019. The Influence of Geometrical and
517 Operational Parameters on Internal Flow Characteristics of Internally Mixing Twin-Fluid Y-Jet
518 Atomizers. *Atomizations & Sprays,* 59(5), pp. 403-428.

519 Neya, K., Sato, S. & Hatopri, K., 1975. Study of y-jet Twin Flid Atomizer. *Ship Reserach Institute ,* 12(1),
520 pp. 1-19.

521 Nykteri, G. et al., 2020. A Σ-Υ two-fluid model with dynamic local topology detection: Application to
522 high-speed droplet impact. *Journal of Computational Physics,* Volume 408.

523 Okabe, T. et al., 2019. Time-dependent breakup length of liquid sheet in prefiming type of airblast
524 atomizer. *Atomization & Sprays,* 29(1), pp. 289-303.

525 Pacifico, A. L. & Yanagihara, J. I., 2014. The influence of geometrical and operational parametrs on Y-
526 jet atomizers performance. *Journal of Brazilian Society of Mechanical Science and Engineering,*
527 Volume 36, pp. 13-32.

528 Piomelli, U. & Balaras, E., 2002. Wall-layer Models for Large-Eddy Simulations. *Annual Review of Fluid*
529 *Mechanics ,* Volume 34, pp. 349-374.

530 Prasad, K. S. L., 1982. *Characterization of Air Blast Atomizers.* madison wisconsin, International
531 Conference on Liquid Atomization and Spray Systems.

532   Ranz, W. E. & Marshall, W. R., 1952 a. Evaporation from drops, Part 1. *Chemical Engineering*
533   *Progress,* 48(3), pp. 141-146.

534   Ranz, W. E. & Marshall, W. R., 1952 b. Evaporation from Drops Part 1 and Part 2. *Chemical*
535   *Engineering Progress,* 48(4), pp. 173-180.

536   Roesler, T. C. & Lefebvre, A. H., 1989. Studies on aerated-liquid atomization. *International journal of*
537   *turbojet engines,* Volume 6, pp. 221-230.

538   Roudini, M. & Wozniak, G., 2018. Experimental Investigation of Spray Characteristics of Pre-Filming
539   Air-blast Atomizers. *Journal of Applied Fluid Mechanics,* 11(6), pp. 1455-1469.

540   Sami, M., Schuetze, P., Hutcheson, P. & Aguado, P., 2019. *Best Practices in the numerical modelling of*
541   *liquid atomization processes.* Tempe, Arizona, ILASS-Americas 30th Annual Conference on Liquid
542   Atomization and Spray System.

543   Schtze, J. et al., 2018. *A multimodel hybrid approach for the numerical simulation of fluid phase*
544   *dispersion process.* Chicago, International Conference on Liquid Atomization and Sprays Systems.

545   Shur, M. L., Spalart, P. R., Strelets, M. K. & Travin, A. K., 2008. A hybrid RANS-LES approach with
546   delayed-DES and wall-modelled LES capabilities. *International Journal of Heat and Fluid Flow,* Volume
547   29, pp. 1638-1649.

548   Shur, M., Strelets, P., Spalart, M. & Travin, A., 1999. Detached-eddy simulation of an airfoil at high
549   angle of attack. *Engineering Turbulence Modeling and Measurements,* Volume 4, pp. 669-678.

550   Smagorinsky, J., 1963. General Circulation Experiments with the Primitive Equations. *Monthly*
551   *Weather Review,* Volume 91, pp. 99-165.

552   Song, S. H. & Lee, S. Y., 1996. Study of Atomization Mechanism of Gas/Liquid Mixtures Flowing
553   Through Y-Jet Atomizers. *Atomization and Sprays,* Volume 6, pp. 193-209.

554   Song, S. & Lee, S., 1994. *An Examination of Spraying Performance of Y-Jet Atomizers- Effect of Mixing*
555   *Port Length.* Rouen, International Conference on Liquid Atomization and Spray Systems.

556   Sovani, S. D., Sojka, P. E. & Lefebvre, A. H., 2001. Effervescent Atomization. *Progress in Energy and*
557   *Combustion Sciences,* Volume 27, pp. 483-521.

558   Stefanitsis, D. et al., 2019b. Numerical investigation of the aerodynamic breakup of droplets in
559   tandem. *International Journal of Multiphase Flow,* Volume 113, pp. 289-303.

560   Stefanitsis, D., Strotos, G., Nikolopoulos, N. & Gavaises, M., 2019a. Numerical investigation of the
561   aerodynamic breakup of a parallel moving droplet cluster. *International Journal of Multiphase Flow,*
562   Volume 121.

563   Strotos, G. et al., 2011. Non-dimensionalisation parameters for predicting the cooling effectiveness of
564   droplets impinging on moderate temperature solid surfaces. *International Journal of Thermal*
565   *Sciences,* Volume 50, pp. 698-711.

566   Strotos, G., Malgarinos, I., Nikolopoulos, N. & Gavaises, M., 2016a. Aerodynamic breakup of an n-
567   decane droplet in a high temperature gas environment. *FUEL,* Volume 185, pp. 370-380.

568   Strotos, G., Malgarinos, I., Nikolopoulos, N. & Gavaises, M., 2016b. Predicting droplet deformation
569   and breakup for moderate Weber numbers. *International Journal of Multiphase Flow,* Volume 85, pp.
570   96-109.

571 Strotos, G. et al., 2018. Determination of the aerodynamic droplet breakup boundaries based on a
572 total force approach. *International Journal of Heat and Fluid Flow,* Volume 69, pp. 164-173.

573 Tonini, S., Gavaises, M. & Theodorakakos, A., 2008. Modelling of high-presure dense diesel sprays
574 with adaptive local grid refinement. *International journal of Heat and Fluid Flows,* Volume 29, pp.
575 427-448.

576 Vallet, A., Burluka, A. A. & Borghi, R., 2001. Development of a Eulerian model for the 1168
577 "atomization" of a liquid jet. *Atomization and Sprays,* 11(6).

578 Van Driest, E. R., 1956. On Turbulent flow near a wall. *Journal of Aeronautical Sciences,* Volume 23,
579 pp. 1007-1011.

580 Zhou, X., Li, T. & Lai, Z., 2019 b. Similarity of split-injected fuel sprays for different size diesel engines.
581 *International Journal of Engine Research.*

582 Zhou, X., li, T., Wei, Y. & Wang, N., 2019 a. Scaling liquid penetration in evaporating sprays for
583 different size diesel engines. *International Journal of Engine Research.*

584

585

586

587

588

589

590

591

592

593

594

595

596

597

Appendix I. Grid Independent Study

598

599   A grid independence study was conducted to check whether the drop size distribution measured

600   along the Y axis on the plane A change with the mesh. Two different dynamic solution-adaptive mesh

601   refinements were used through PUMA method. Mesh "I" has three levels of dynamic mesh

602   refinement and minimum cell volume of $10^{-16}\ m^3$, while Mesh "II" has three levels of dynamic mesh

603   refinement and minimum cell volume of $10^{-17}\ m^3$. Average SMD distribution for the momentum

604   rations (φ) 3.2, 7.3 and 9.4 for one hundred thousand time steps are shown in the Figure 9(a), Figure

605   9(b) and Figure 9(c) respectively. The drop size distribution for both the meshes is almost the same.

606   Figure 10 shows the contour of the average volume fraction of the light fuel oil within the nozzle over

607   one hundred thousand time steps for the Mesh "I" and Mesh "II" for the momentum rations (φ) of

608   3.2, 7.3 and 9.4. The average volume fraction for both the meshes for the momentum ratios of 3.2

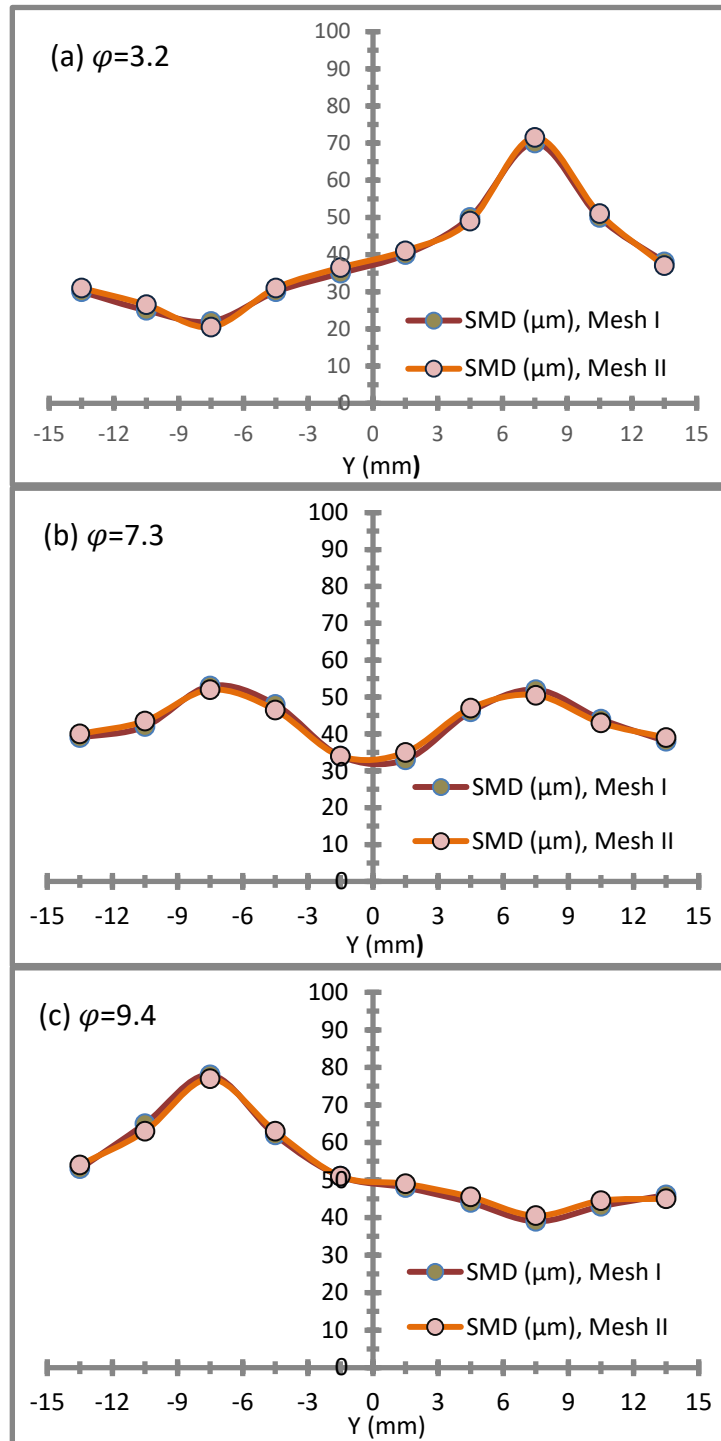609   (figure a & b), 7.3 (figure c & d) and 9.4 (figure e & f) are almost the same.

610

611

612

613

614

615

616

617

618

619

Figure 9 SMD drop size distribution for MESH I and MESH II for the liquid-to-gas momentum ratios of (a) 3.2, (b) 7.3, and (c) 9.4.

Average Volume Fraction of Light Fuel Oil

0.0   0.3   0.6   1.0

(a) Mesh I, φ=3.2

(b) Mesh II, φ=3.2

(c) Mesh I, φ=7.3

(d) Mesh II, φ=7.3

(e) Mesh I, φ=9.4
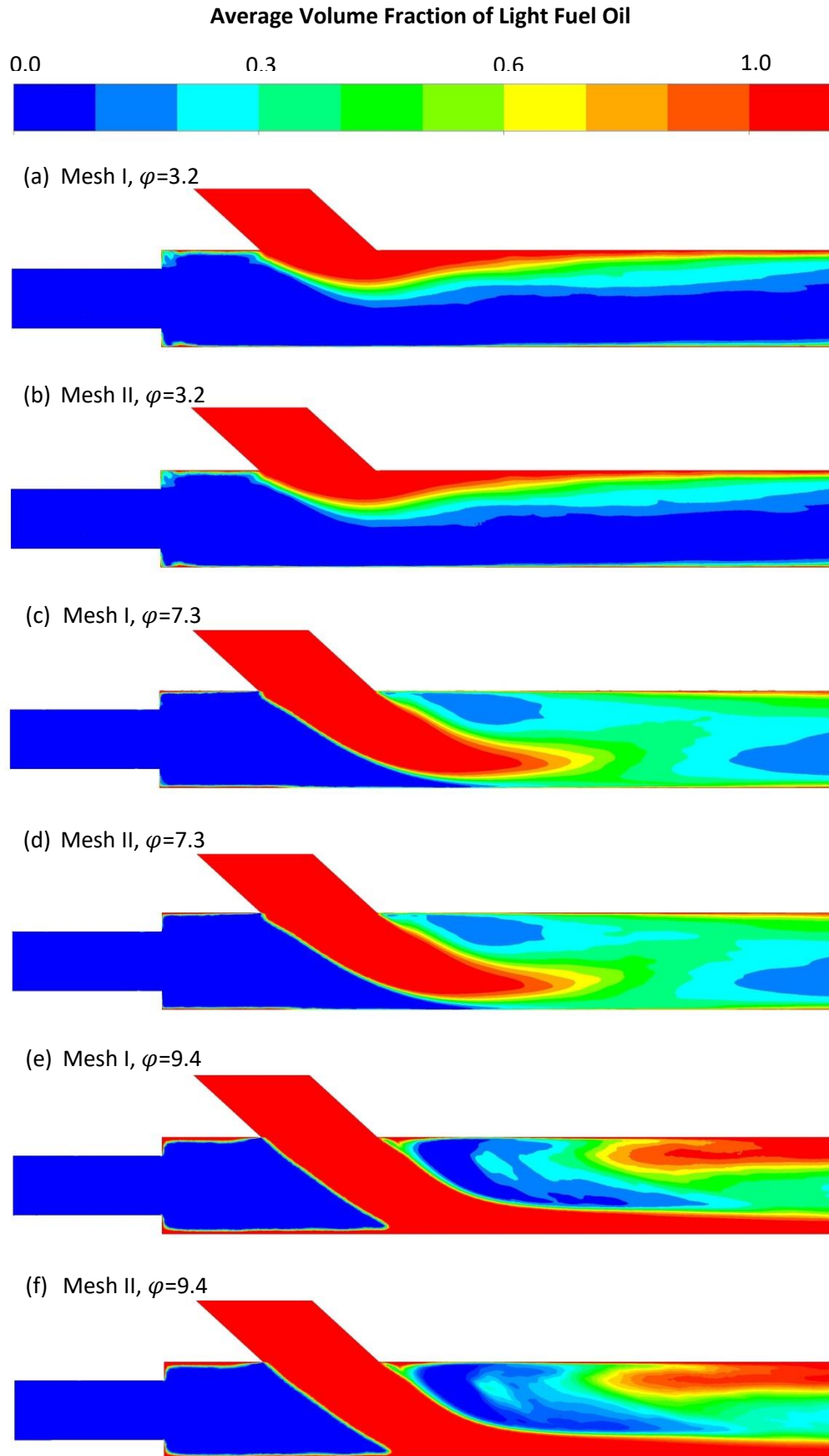
(f) Mesh II, φ=9.4

Figure 10 Average volume fraction of light fuel oil over one hundred time steps for liquid-to-gas momentum ratios of 3.2 (a) Mesh 'I' (b) Mesh 'II', 7.3 (c) Mesh 'I' (d) Mesh 'II' and 9.4 (e) Mesh 'I' (f) Mesh 'II'.

Appendix II. Asphericity Independent Study

680

681   Figure 11 shows the contour of the average volume fraction of the light fuel oil within the nozzle over

682   one hundred thousand time steps for asphericity of 0.01 and 2.5 for the momentum ratio (φ) of 2.8.

683   The average volume fraction for both the asphericities (figure a & b) are almost the same.
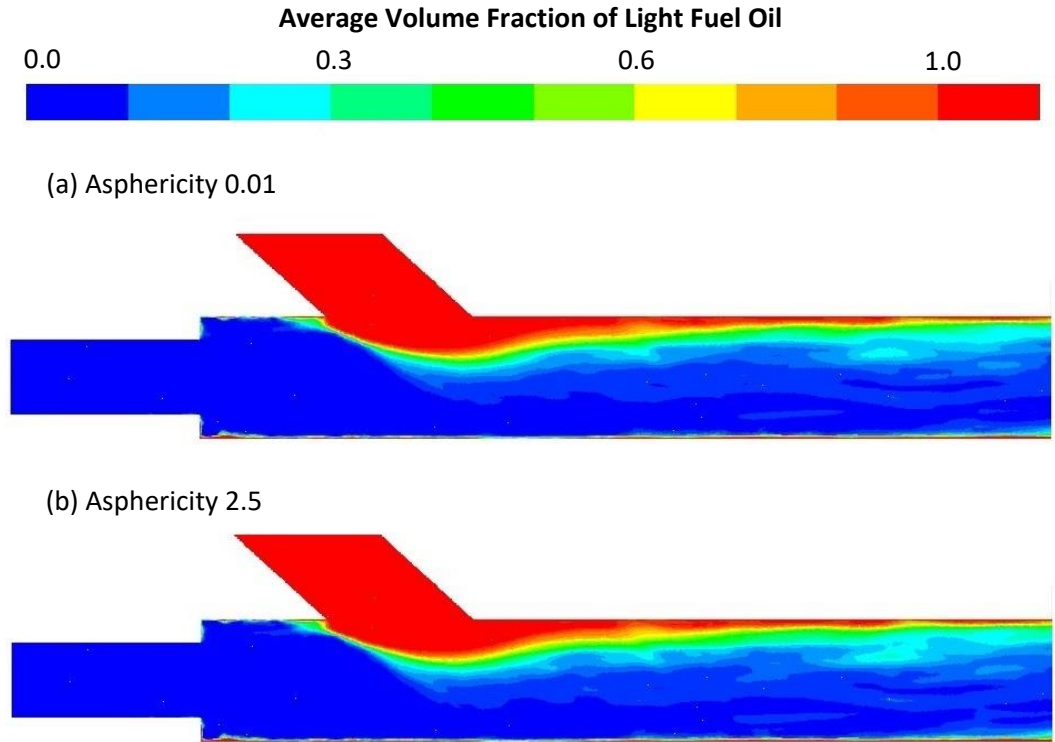
684

685

686

687

688

Figure 11 Average volume fraction of light fuel oil over one hundred time steps for asphericity ratios of (a) 0.01 and (b) 2.5 for the liquid-to-gas momentum ratio of 2.8.